Science Press

ARTICLE

Macroscopic and Microscopic Residual Stress in Single Shot Impacted Pure Titanium

Wang Yaomian,   Yang Huanping,   Zhuang Wei,   Yan Wenbin

School of Metallurgical Engineering, Xi'an University of Architecture and Technology, Xi'an 710055, China

Abstract: The finite element method (FEM) and elasto-plastic self-consistent (EPSC) method were used to simulate the mechanical response of pure titanium subjected to single steel shot impacting at different shot sizes and velocities. The macroscopic and microscopic residual stresses were calculated. The results indicate that the observed macroscopic compressive residual stress increases with the increase of the shot size and impacting velocity. In addition, the macroscopic residual stress calculations correlate well with the residual elastic strain. The microscopic residual stresses lie within a range that varies with depth. Furthermore, the statistical distribution of the microscopic residual stress agrees well with the Gaussian distribution. Additionally, the dispersion of microscopic residual stresses, determined by the effective plastic deformation, is influenced by the shot size and impacting velocity. With the increase of the impacting velocity and decrease of the shot size, the standard deviation of the microscopic residual stress distribution increases at a certain depth.

Key words: residual stress; finite element; impacting; plastic deformation; titanium

Residual stresses have a significant influence on mechanical performance and are present in many structures and components. According to their action scale, residual stress can be divided into macroscopic (type Ⅰ) and microscopic (type Ⅱ and type Ⅲ) stresses[1-3]. Type Ⅰ residual stress is the volume average of the position-dependent residual stresses. The volume has to be large enough to include numerous grains for representing the macroscopic materials; therefore, type Ⅰ residual stress can induce macroscopic dimensional change. Type Ⅱ residual stress is the deviation from the type Ⅰ residual stress for an individual grain. It is an intergranular stress caused by grain interaction and varies from grain to grain. Type Ⅱ residual stress is also called a homogeneous microstress. Type Ⅲ residual stress is an intragranular stress, which represents the local variation within a grain due to dislocations, or other lattice defects. Type Ⅲ residual stress is referred to an inhomogeneous microstress. Clearly, the actual residual stress at a specific location is the sum of the three types of residual stresses.

In order to improve the mechanical properties of engineering materials and components, the compressive residual stress can be introduced through many types of processes, such as conventional shot peening[4, 5], laser shock peening[6-8], surface mechanical attrition treatment[9, 10], surface mechanical rolling treatment[11], and ultrasonic surface rolling processing[12]. The fatigue life[13, 14], strength[15, 16], hardness[17], and stress corrosion resistance[3] can be enhanced significantly due to the resulted residual stress. Usually, it is considered that the compressive residual stress can lower the tensile stress level applied by the external loading, inhibit the crack nucleation in the surface layer, and accelerate the closure of the fatigue crack[18]. Extensive research has been conducted to characterize the macroscopic compressive residual stress[3, 19], elucidate the influence of processing on macroscopic residual stress[20], and investigate the relationship between the macroscopic residual stress and microstructure[9]. However, some issues, such as the formation mechanism of the macroscopic residual stress and its control, as well as

correlation of the macroscopic and microscopic residual stress, are still unclear.

Similar to the macroscopic residual stress, microscopic residual stress also shows significant influence on the properties and performance of a material; for instance, short crack propagation[3], micro-crack formation[21], and stress-induced transformation[22]. Microscopic residual stress in grains with specific planes can be measured using neutron diffraction[23] and X-ray microbeam diffraction[22]. The image correlation approach is also used to characterize the residual stress in micro-scale[24]. Residual stress in individual grain can be measured by utilizing the electron back scatter diffraction (EBSD) method[25, 26]. Though different methods have been employed to measure the microscopic residual stress, their mechanisms are still ambiguous. Further investigations are needed to elucidate the distribution characteristics of the microscopic residual stress and their influence mechanism.

In order to elucidate the related underlying mechanism of residual stress induced by shot impacting, many researches have been conducted by using finite element method (FEM)[9,27-29]. In these researches, the macroscopic residual stresses induced by a single shot and by multiple balls were compared. It is shown that these residual stress distributions are similar. Therefore, in the present study, a single shot impacting was employed. The effects of velocity and shot size on the macroscopic and microscopic residual stresses were examined through FEM and elasto-plastic self-consistent (EPSC) model. Based on the calculation, the influence mechanisms were analyzed.

1 FE Model and Validation

The impacts were simulated by the commercial finite element code ABAQUS, using a 3D symmetry model shown in Fig.1. A target with dimensions of 2 mm × 2 mm × 4 mm was used. A C3D8R 8-node linear brick element with reduced integral and hourglass control was utilized for the target. A mesh, fine near the contact region and gradually coarser further away, was employed to ensure numerical accuracy and calculation efficiency. Only one quarter of the steel shot was modeled because of symmetry. A C3D4 4-node linear tetrahedron element was employed for the shot. The steel shot was assumed to be rigid during the impacting. A kinematic contact method was adopted for the interaction between the shot surface and the top surface of the target. In the FE model, the center of the bottom surface was set as the origin of the coordinate system. During simulation, symmetry displacement conditions were applied on the $y=1$ mm and $x=1$ mm planes. Furthermore, the bottom surface was fixed.

To validate the FE model, a comparison with the study conducted by Meguid et al[27] was made. In their research, a high-strength steel target was impacted by a steel shot with a diameter of 1 mm and impacting velocity of 50 m·s^{-1}. Fig.2 shows the variation in the normalized residual stress σ_{xx}^r/σ_0
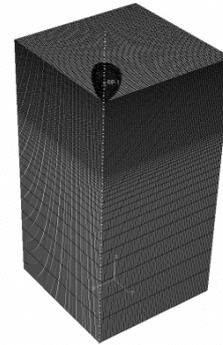
Fig.1   FE model for single shot impacting
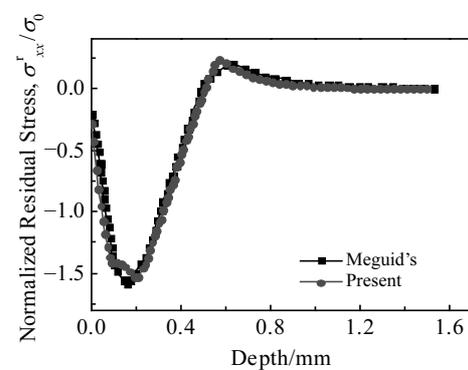
Fig.2   Comparison of the residual stress in steel target computed by Meguid's and the present FE model

with depth for both Meguid's and the present study. Here, σ_{xx}^r is the residual stress on the x axis, and σ_0 is the initial yield stress. The calculation results are very close, which validate that the present FE analysis is feasible to some extent.

The stress-strain relationship of pure titanium is shown in Fig.3 and the material parameters are summarized in Table 1. Steel shots with a diameter of 0.5 mm and 1.0 mm were employed in the simulation. Four different impacting velocities were used: 30, 50, 70, and 90 m·s^{-1}.
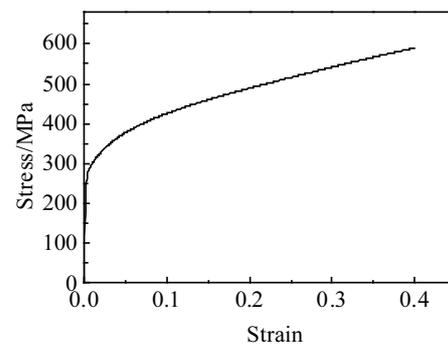
Fig.3   Stress-strain relationship used for pure titanium

Table 1   Material parameters used in the FEM calculation

	Density/kg·m^{-3}	Elastic modulus/GPa	Poisson's ratio
Target	4510	114.8	0.32
Steel shot	7800	200.0	0.26

2   EPSC Model

An EPSC polycrystal model has been utilized to investigate the mechanical response[30-32], internal lattice strain[32-35], residual stress[34-36], and texture evolution[33, 34, 36]. In the EPSC model, each grain is regarded as an inclusion within a homogeneous medium.

During plastic deformation, the stress rate $\dot{\sigma}$ and total strain rate $\dot{\varepsilon}$ of the polycrystals can be expressed with the following equation:

$$\dot{\sigma} = L : \dot{\varepsilon} \tag{1}$$

where L represents the overall instantaneous elasto-plastic stiffness tensor.

The similar constitutive relation of a particular grain is given by:

$$\dot{\sigma}^c = L^c : \dot{\varepsilon}^c \tag{2}$$

where $\dot{\sigma}^c$ and $\dot{\varepsilon}^c$ are the stress rate and strain rate of the grain, respectively. Additionally, L^c is the grain modulus, which depends on the grain orientation, the single crystal elastic constants, and the plastic state of the grain.

According to Eshelby's equivalent inclusion model, the relationship between the total strain rate in a grain and that in the bulk medium is described by the following:

$$\dot{\varepsilon}^c = A^c : \dot{\varepsilon} \tag{3}$$

where A^c is the localization tensor, and it is given by:

$$A^c = (L^c + L^*)^{-1} : (L + L^*) \tag{4}$$

where L^* is called the effective stiffness, and it is given by the following:

$$L^* = L : (S^{-1} - I) \tag{5}$$

where S is the elasto-plastic Eshelby tensor, and I is the fourth order unity tensor.

To satisfy the self-consistent condition, the weighted averages of stress rate and strain rate of all the constituent grains have to coincide with the macroscopic magnitudes of the polycrystals:

$$\dot{\varepsilon} = \left\langle \dot{\varepsilon}^c \right\rangle \tag{6}$$

$$\dot{\sigma} = \left\langle \dot{\sigma}^c \right\rangle \tag{7}$$

Macroscopic elasto-plastic stiffness can be expressed as:

$$L = \left\langle L^c : A^c \right\rangle \tag{8}$$

Given a macroscopic stress or strain increment, a new estimate of L can be determined by an iterative procedure. In this procedure, the stress and strain of each grain can be calculated. Samples consisting of 2000 grains with typical hot rolled textures were employed in the present EPSC simulation.

Prismatic slip $\{10\bar{1}0\} < \bar{1}2\bar{1}0 >$, pyramidal slip $\{10\bar{1}1\} < \bar{1}\bar{1}23 >$, base slip $\{0002\} < 2\bar{1}\bar{1}0 >$, tensile twining $\{10\bar{1}2\} < \bar{1}011 >$, and compressive twining $\{2\bar{1}\bar{1}2\} < 2\bar{1}\bar{1}3 >$ were selected as the deformation systems for pure

titanium[37-39]. A voce hardening model was used to describe the relationship between threshold shear stress τ and accumulated shear strain Γ for a deformation system in one grain:

$$\tau = \tau_0 + (\tau_1 + \theta_1 \Gamma)(1 - \exp(-\theta_0 \Gamma / \tau_1)) \tag{9}$$

where τ_0, τ_1, θ_0 and θ_1 are the hardening parameters. Through comparison of the tensile stress-strain curve and texture evolution character[37,40], the hardening parameters of each deformation mode are determined and listed in Table 2. The single-crystal elastic constants used in this model are $C_{11} = C_{22} = 162.4$ GPa, $C_{33} = 180.7$ GPa, $C_{12} = 92$ GPa, $C_{13} = 69$ GPa, and $C_{44} = 46.7$ GPa.

In the present study, explicit dynamic FE simulation of the single shot impacting was first conducted. The macroscopic strain of the target, at the moment when the shot velocity decreased to zero, was obtained. Whereafter, general statistic simulation was carried out to obtain the residual strain and residual stress at macroscopic scale. Following the simulation, the EPSC calculation was conducted with strain control. The loading and unloading conditions were determined according to the FE simulations. In the EPSC calculation, macroscopic residual stress of the samples at different depths and the actual residual stress of each grain can be determined.

3   Results and Discussion

3.1   Macroscopic residual stress distribution

In this study, the macroscopic residual stresses in pure titanium, impacted by a single shot with different velocities and diameters, were calculated through both the FE and EPSC method. Fig.4 shows the variation in the macroscopic residual stress on the X axis with depth from the impacted surface. The residual stresses calculated by the two methods show a similar variation with depth for different impacting velocities and shot sizes, as observed in Fig.4. In addition, the two methods exhibit good agreement, except in the region near the maximum residual stress.

As the impacting velocity increases, the dynamic energy increases, which induces more severe plastic deformation in titanium. As a result, the calculated residual stress increases with the impacting velocity as shown in Fig.4. For the smaller

Table 2   Hardening parameters used in EPSC simulation (MPa)

Deformation mode	τ_0	τ_1	θ_0	θ_1
Prismatic slip $\{10\bar{1}0\} < \bar{1}2\bar{1}0 >$	65	20	260	10
Pyramidal slip $\{10\bar{1}1\} < \bar{1}\bar{1}23 >$	410	20	500	73
Base slip $\{0002\} < 2\bar{1}\bar{1}0 >$	155	30	700	75
Tensile twining $\{10\bar{1}2\} < \bar{1}011 >$	65	10	90	70
Compressive twining $\{2\bar{1}\bar{1}2\} < 2\bar{1}\bar{1}3 >$	90	150	1900	325
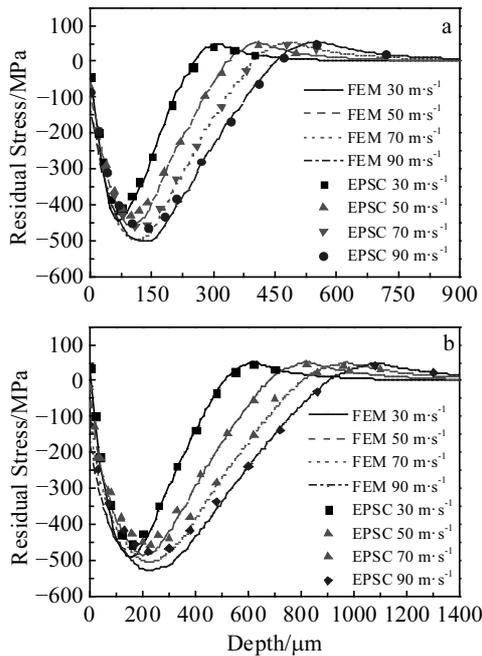
Fig.4   Macroscopic residual stress induced by steel shot impacting with a diameter of 0.5 mm (a) and 1.0 mm (b)

shot with a diameter of 0.5 mm, the depth of the compressive stress field increases from 250 μm to 450 μm as the impacting velocity increases from 30 m·s⁻¹ to 90 m·s⁻¹. Furthermore, the maximum compressive residual stress increases from 443 MPa to 500 MPa and the corresponding depth where the maximum compressive residual stress occurs also increases from 70 μm to 140 μm.

With increasing the shot size, the dynamic energy during shot impacting also increases. Consequently, the residual stress field grows, as shown in Fig.4. In Fig.4, it can be seen that the depth of the residual stress field, the maximum residual stress, and its corresponding depth increase at different impacting velocities as the shot size increases from 0.5 mm to 1.0 mm. In addition, it should be noted that the contact area between the shot and the target increases with the increase in the shot size. Consequently, the coverage rate increases after the impacting from a larger shot. However, the enhancement in the residual stress field is not so distinct with increasing impacting velocity, as observed for the smaller shot. As the velocity increases from 30 m·s⁻¹ to 90 m·s⁻¹, the depth of the residual stress field and the maximum residual stress increase by 7% and 76%, respectively; whereas, the corresponding increment is 13% and 80% for the smaller shot.

During the shot impacting, plastic deformation along the depth direction is inhomogeneous. As a result, residual elastic strain is also inhomogeneous. The calculated residual elastic normal strain on the X axis for the single shot impacting is shown in Fig.5. From Fig.5, one can observe that the amount

of residual elastic strain is small in the surface layer. With increasing depth, the residual elastic strain increases significantly. In the subsurface layer, the residual elastic strain exhibits the maximum value. Subsequently, the strain decreases gradually. The deformation during impacting and the relief of the elastic strain during rebounding of the shot both determine the distribution characteristics of the residual elastic strain. Correlation can be observed when comparing residual elastic strain with the distribution of macroscopic residual stresses.

3.2   Microscopic residual stress

According to the residual stress classification, the relationship among the macroscopic, microscopic, and actual residual stress in an individual grain can be expressed by:

$$\sigma_i^{\mathrm{r,gr}} = \sigma^{\mathrm{r,mac}} + \sigma_i^{\mathrm{r,mic}} \tag{10}$$

$$\sigma^{\mathrm{r,mac}} = \frac{1}{N} \sum_{i=1}^{N} \sigma_i^{\mathrm{r,gr}} \tag{11}$$

where $\sigma_i^{\mathrm{r,gr}}$ represents the actual residual stress in the ith grain, $\sigma_i^{\mathrm{r,mic}}$ is the microscopic residual stress of the ith grain, and $\sigma^{\mathrm{r,mac}}$ is the macroscopic residual stress of the component composed of N grains. Through the EPSC method, the actual residual stress in each grain after the single shot impacting was calculated. Due to the difference in the crystal orientation, residual stress of the individual grain varies from one grain to another, even though they are subjected to the same macroscopic mechanical loading. Fig.6 shows the actual residual stress distribution along the depth direction for the grains under different impacting conditions. Clearly, it can be found that the actual residual stresses of the grains at a certain
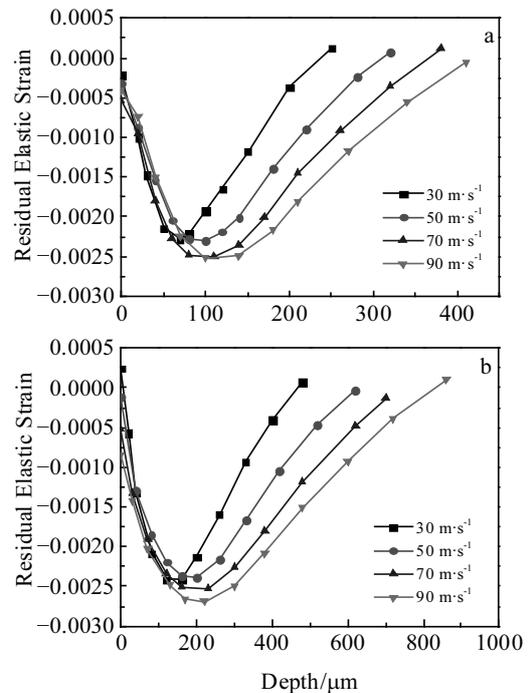
Fig.5   Residual elastic strain induced by steel shot impacting with a diameter of 0.5 mm (a) and 1.0 mm (b)
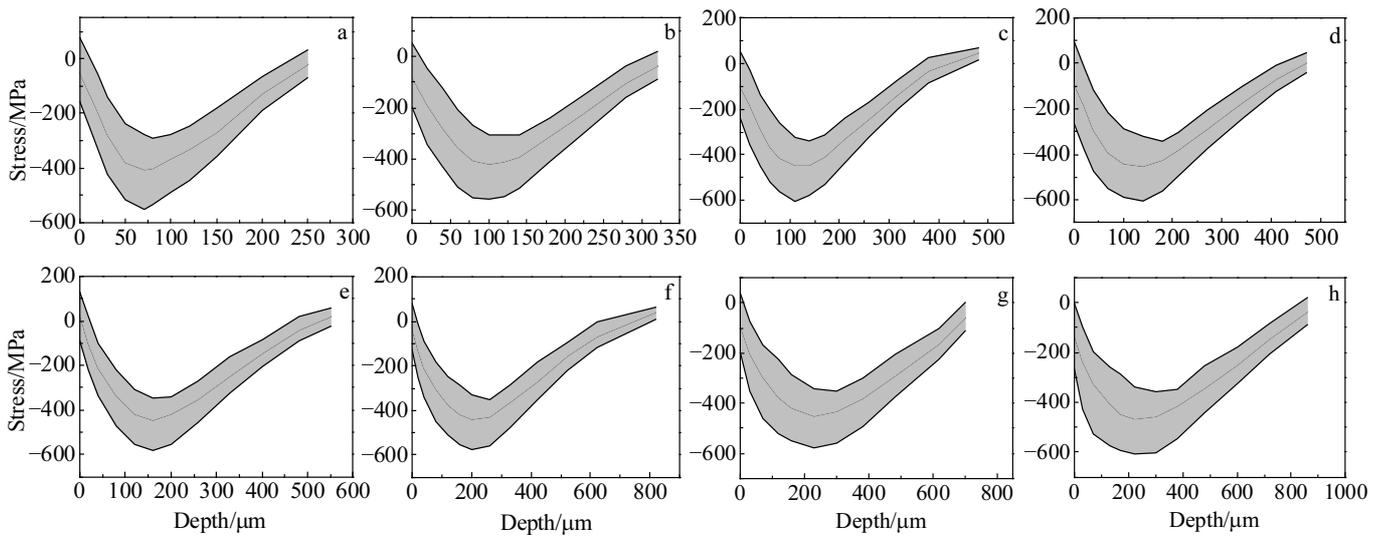
Fig.6   Distributions of the actual residual stress in grains at varying depths, for the samples impacted by a steel shot at different shot sizes and velocities: (a) 0.5 mm, 30 m·s⁻¹; (b) 0.5 mm, 50 m·s⁻¹; (c) 0.5 mm, 70 m·s⁻¹; (d) 0.5 mm, 90 m·s⁻¹; (e) 1.0 mm, 30 m·s⁻¹; (f) 1.0 mm, 50 m·s⁻¹; (g) 1.0 mm, 70 m·s⁻¹; (h) 1.0 mm, 90 m·s⁻¹

depth lie within a wide range. Computing the average of the actual grain residual stresses at a certain depth, according to Eq.(11), it shows that this average is equal to the macroscopic residual stress, as shown in Fig.4.

According to Eq.(10), the microscopic residual stress in each grain can be calculated. Fig.7 shows the distribution of microscopic residual stress for the grains after single shot impacting. The microscopic residual stress varies from one grain to another, and the microscopic residual stresses lie within a range that is dependent on depth. With increasing impacting velocity and shot size, the distribution characteristics of the microscopic residual stress show distinct variation.

In order to illustrate the distribution characteristics of the microscopic residual stress, a Gaussian distribution was employed, which is given by:

$$y = y_0 + \frac{A}{w\sqrt{\pi/2}} e^{-2\frac{(x-x_c)^2}{w^2}} \tag{12}$$
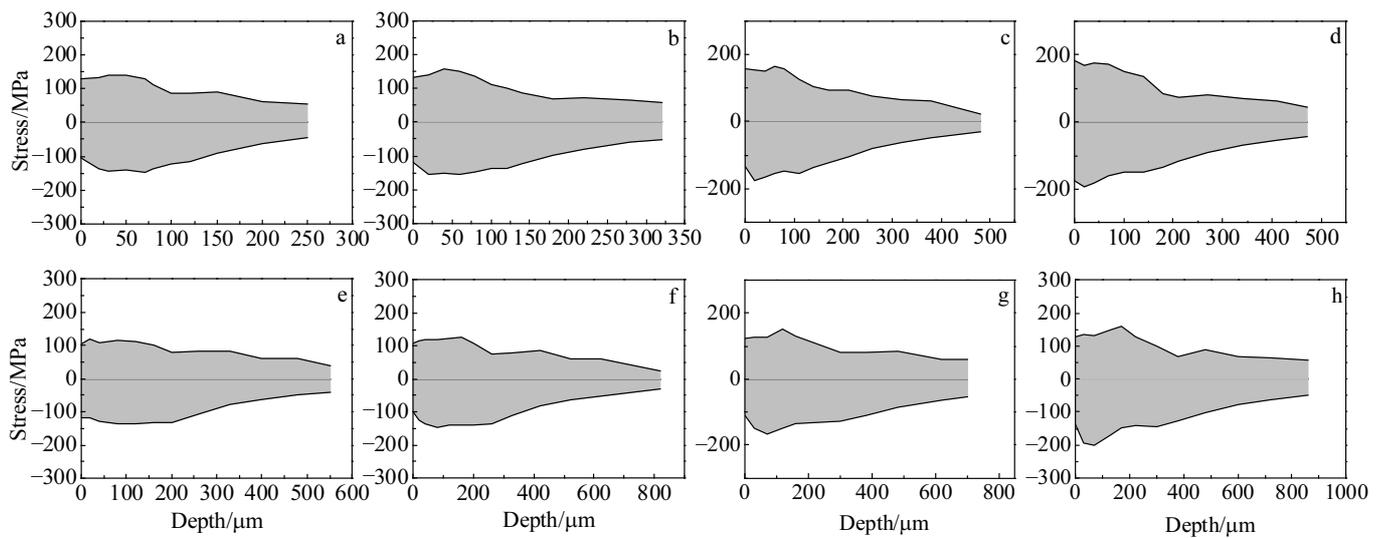
Fig.7   Distributions of the microscopic residual stress at varying depths, for the samples impacted by a steel shot at different shot sizes and velocities: (a) 0.5 mm, 30 m·s⁻¹; (b) 0.5 mm, 50 m·s⁻¹; (c) 0.5 mm, 70 m·s⁻¹; (d) 0.5 mm, 90 m·s⁻¹; (e) 1.0 mm, 30 m·s⁻¹; (f) 1.0 mm, 50 m·s⁻¹; (g) 1.0 mm, 70 m·s⁻¹; (h) 1.0 mm, 90 m·s⁻¹

where y is the distribution frequency or probability density, y_0 represents the offset, x_c is the average of variable x, A is a coefficient, and $w=2$ s. Here, s represents the standard deviation which is a measure of the dispersion of the variables relative to their average.

The statistical analysis shows that the microscopic residual stresses, for the grains at a certain depth from the surface, agree well with the Gaussian distribution. For example, Fig.8 gives the statistical distribution of the microscopic residual stress at the depth where the maximum macroscopic residual stress occurred for the titanium sample impacted by a steel shot at 30 m·s^{-1}, and a size of 0.5 mm. As shown in Fig.8, the distribution of the microscopic residual stresses exhibits a bell shaped curve. The statistical analysis indicates that 80.1% of the grains show a small magnitude of microscopic residual stress less than 50 MPa, but 3.2% of the grains show a distinct microscopic residual stress magnitude greater than 100 MPa.

The variations in standard deviation of the microscopic residual stresses with depth at varying impacting velocities and shot sizes are shown in Fig.9. Fig.9 shows that standard deviation increases with depth in the surface layer. Subsequently, deviation decreases gradually and reaches a stable value. Furthermore, impacting velocity has an important influence on the standard deviation. With increasing velocity, the standard deviation increases significantly, and the depth where the standard deviation stabilizes is deeper. This indicates that the microscopic residual stresses spread over a wider range as the impacting velocity increases. With increasing shot size, the maximum standard deviation decreases for the varying impacting velocities. However, both the depth where the maximum standard deviation occurred and the depth where the standard deviation stabilized underwent a substantial increase. For example, these two depths are about 20 and 150 μm, respectively for the small shot at an impacting velocity of 30 m·s^{-1}, and they increases to about 80 and 260 μm, respectively, as the shot size increases to 1.0 mm.

Through comparison with the distribution of macroscopic residual stress shown in Fig.4, it can be seen that the depth
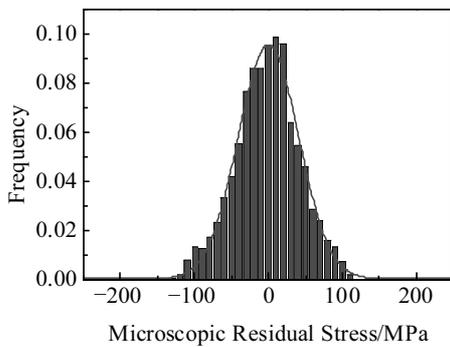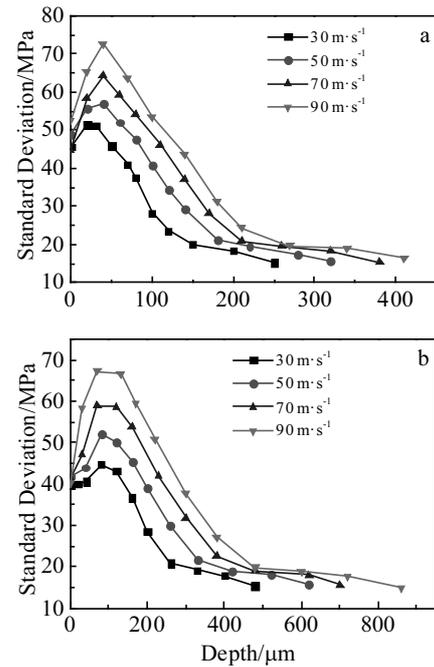
Fig.9   Variations of the standard deviation of the microscopic residual stress with depth for the samples impacted by steel shot with a diameter of 0.5 mm (a) and 1.0 mm (b)

corresponding to the maximum macroscopic residual stress is about two times larger than the one corresponding to the maximum standard deviation of the microscopic residual stress. Microscopic residual stress results from the heterogeneous plastic deformation among the grains; therefore, the stress should be influenced by the plastic deformation level. Due to the complexity of the strain state, an effective plastic strain is introduced, which is given by:

$$\varepsilon_p = \sqrt{\frac{2}{3}\varepsilon_{ij}^p \varepsilon_{ij}^p} \tag{13}$$

where ε_{ij}^p is the plastic strain component. The computed effective plastic strain is shown in Fig.10. Clearly, it can be found that the effective plastic strain ε_p and the corresponding standard deviation of the microscopic residual stresses show consistent variation with depth.

From Eq.(3), it can be deduced that the plastic strain in a grain is proportional to the macroscopic plastic strain. The grains with soft orientation undergo high plastic deformation, while the grains with hard orientation experience small plastic deformation. As the macroscopic plastic deformation increases, discrepancy in the plastic deformation of the grains with different orientations increases. Therefore, standard deviation of the microscopic residual stress becomes large. With increasing impacting velocity, the plastic deformation level of the titanium target increases, as shown in Fig.10. Consequently, a more distinct dispersion of the microscopic residual stress is induced. As the shot size increases from 0.5 mm to

Fig.8   Statistical distribution of the microscopic residual stress
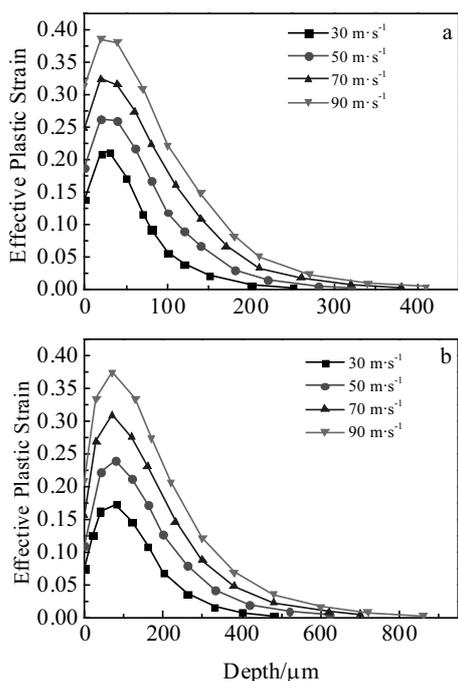
Fig.10   Variations of the effective plastic strain with depth for the samples impacted by steel shot with a diameter of 0.5 mm (a) and 1.0 mm (b)

1.0 mm, though the kinetic energy of the shot increases, the contact area between the shot and the target also increases. As a result, the effective plastic deformation shows a decline, as Fig.10 shows. Accordingly, the standard deviation of the microscopic residual stresses decreases with increasing shot size.

4   Conclusions

1) With increasing shot size and impacting velocity, the impacting dynamic energy increases. Thus, a more significant residual stress field is induced. The macroscopic residual stress and residual elastic strain exhibit an approximate variation with depth for the different impacting parameters.

2) The microscopic residual stresses lie within a wide range because of the heterogonous plastic deformation in the grains with different orientations. All of the microscopic residual stress at a certain depth agree well with the Gaussian distribution.

3) The dispersion of the microscopic residual stress, represented by the standard deviation, is determined by the effective plastic deformation. As impacting velocity increases and shot size decreases, the effective plastic deformation increases; consequently, the standard deviation of the microscopic residual stress becomes larger.

References

1   Hauk V. *Structural and Residual Stress Analysis by Nondestructive Methods*[M]. Amsterdam: Elsevier Science B V, 1997: 59

2   Wang Y D, Peng R L, Wang X L *et al. Acta Materialia*[J], 2002, 50(7): 1717

3   Withers P J. *Reports on Progress in Physics*[J], 2007, 70(12): 2211

4   Wang S P, Li Y J, Yao M *et al. Journal of Materials Processing Technology*[J], 1998, 73(1-3): 64

5   Gao Y K, Yao M, Li J K. *Metallurgical and Materials Transactions A*[J], 2002, 33(6): 1775

6   Zhang X C, Zhang Y K, Lu J Z *et al. Materials Science and Engineering A*[J], 2010, 527(15): 3411

7   Maawad E, Sano Y, Wagner L *et al. Materials Science and Engineering A*[J], 2012, 536: 82

8   Sun R J, Li L H, Zhu Y *et al. Modelling and Simulation in Materials Science and Engineering*[J], 2017, 25(6): 65 016

9   Wang Y M, Yang H P, Zhang C H *et al. Metals and Materials International*[J], 2015, 21(2): 260

10   Zhou J, Retraint D, Sun Z *et al. Surface and Coatings Technology*[J], 2018, 349: 556

11   Xin C, Sun Q Y, Xiao L *et al. Journal of Materials Science*[J] 2018, 53(17): 12 492

12   Wang T, Wang D P, Liu G *et al. Applied Surface Science*[J], 2008, 255(5): 1824

13   Webster G A, Ezeilo A N. *International Journal of Fatigue*[J], 2001, 23(S1): 375

14   Wang Y M, Cheng J P, Zhang C H. *Rare Metal Materials and Engineering*[J], 2019, 48(8): 2574 (in Chinese)

15   Steuwer A, Hattingh D G, James M N *et al. Science and Technology of Welding and Joining*[J], 2012, 17(7): 525

16   Wang Y M, Zhuang W, Yang H P *et al. Rare Metals*[J], 2019, 38(9): 824

17   Ma Z S, Zhou Y C, Long S G *et al. Surface and Coatings Technology*[J], 2012, 207: 305

18   Totten G, Howes M, Inoue T. *Handbook of Residual Stress and Deformation of Steel*[M]. Materials Park: ASM International, 2002: 11

19   Withers P J, Bhadeshia H K D H. *Materials Science and Technology*[J], 2001, 17(4): 355

20   Sticchi M, Schnubel D, Kashaev N *et al. Applied Mechanics Reviews*[J], 2015, 67(1): 10 801

21   Archie F, Mughal M Z, Sebastiani M *et al. Acta Materialia*[J], 2018, 150: 327

22   Kwon E P, Sato S, Fujieda S *et al. Materials Science and Engineering A*[J], 2013, 570: 43

23   Gloaguen D, Oum G, Legrand V *et al. Metallurgical and Materials Transactions A*[J], 2015, 46(11): 5038

24   Everaerts J, Salvati E, Uzun F *et al. Acta Materialia*[J], 2018, 156: 43

25   Field D P, Magid K R, Mastorakos I N *et al. Philosophical Magazine*[J], 2010, 90(11): 1451

26   Mikami Y, Oda K, Kamaya M. *et al. Materials Science and Engineering A*[J], 2015, 647: 256

27 Meguid S A, Shagal G, Stranart J C *et al. Finite Elements in Analysis and Design*[J], 1999, 31(3): 179

28 Klemenz M, Schulze V, Rohr I *et al. Journal of Materials Processing Technology*[J], 2009, 209(8): 4093

29 Gariépy A, Larose S, Perron C *et al. International Journal of Solids and Structures*[J], 2011, 48(20): 2859

30 Turner P A, Christodoulou N, Tomé C N. *International Journal of Plasticity*[J], 1995, 11(3): 251

31 Cai S, Daymond M R, Holt R A. *Acta Materialia*[J], 2009, 57(2): 407

32 Kaboli S, Burnley P C. *Materials Science and Engineering A*[J], 2019, 739: 99

33 Neil C J, Wollmershauser J A, Clausen B *et al. International Journal of Plasticity*[J], 2010, 26(12): 1772

34 Gloaguen D, Fajoui J, Girault B. *Acta Materialia*[J], 2014, 71: 136

35 Jia N, Peng R L, Wang Y D *et al. Acta Materialia*[J], 2006, 54(15): 3907

36 Gloaguen D, Berchi T, Girard E *et al. Acta Materialia*[J], 2007, 55(13): 4369

37 Bozzolo N, Dewobroto N, Wenk H R *et al. Journal of Materials Science*[J], 2007, 42(7): 2405

38 Gurao N P, Kapoor R, Suwas S. *Acta Materialia*[J], 2011, 59(9): 3431

39 Guo X D, Seefeldt M. *Journal of Materials Science*[J], 2017, 52(13): 8132

40 Wronski M, Kumar M A, Capolungo L *et al. Materials Science and Engineering A*[J], 2018, 724: 289

单球撞击纯钛的宏观和微观残余应力

王耀勉，杨换平，庄　唯，剡文斌

(西安建筑科技大学 冶金工程学院，陕西 西安 710055)

摘　要：采用有限元法和弹塑性自洽模型模拟纯钛在单个钢球以不同尺寸和速度撞击时的力学响应，计算了宏观和微观残余应力。结果表明，随着钢球尺寸和撞击速度的增加，宏观残余压应力增加。宏观残余应力和残余弹性应变具有较好的一致性。微观残余应力分布在一个随深度变化的范围内。在某一深度处微观残余应力的统计分布符合高斯分布，其离散程度由有效塑性应变决定，有效塑性应变随钢球尺寸和撞击速度变化。增加撞击速度和减小钢球尺寸，在某一深度处微观应力分布的标准差增加。

关键词：残余应力；有限元；冲击；塑性变形；钛

作者简介：王耀勉，男，1983 年生，博士，副教授，西安建筑科技大学冶金工程学院，陕西 西安 710055，电话：029-82202923，E-mail: ymwang@xauat.edu.cn